

pubs.acs.org/IECR Article

# New Approach Lagrangian for Numerical Analysis Within L-V One Equilibrium Stage of a Distillation Column Using the SPH Method

Jazmín Cortez-González, Rodolfo Murrieta-Dueñas,\* Carlos Enrique Alvarado-Rodríguez, Juan Gabriel Segovia-Hernández, Salvador Hernández, and Roberto Gutiérrez-Guerra



Cite This: Ind. Eng. Chem. Res. 2024, 63, 21974–21990



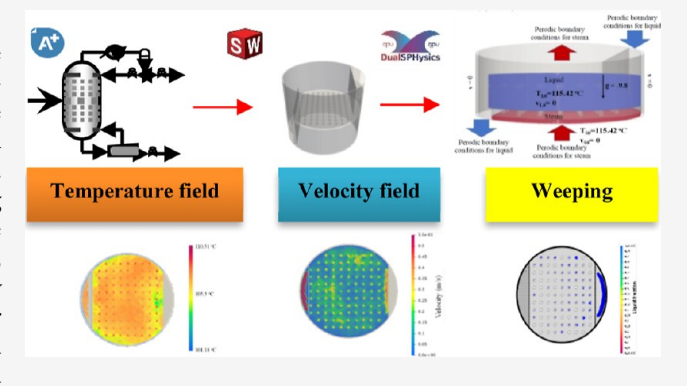
**ACCESS** I

III Metrics & More

Article Recommendations

s Supporting Information

ABSTRACT: This paper presents a numerical analysis of liquid—vapor equilibrium in a sieve tray of a distillation column using the Smoothed Particle Hydrodynamics (SPH) method. This Lagrangian approach provides a comprehensive understanding of the hydrodynamics, heat transfer, and liquid—vapor interactions within the tray, considering variations in deck area (85%, 90%, and 95%). The study examines flow patterns, flow regimes, weeping phenomena, and heat transfer within the tray. Results indicate that with a reduced deck area, the bubble regime predominates, leading to higher weeping rates and lower temperature uniformity between phases. Conversely, increasing the deck area to 90% or 95% shifts the regime to steam jet and spray, reduces weeping, and enhances phase interaction, thereby improving heat transfer and



equilibrium stage efficiency. The study also highlights the effectiveness of the SPH method in simulating complex flow behavior within sieve trays.

#### 1. INTRODUCTION

Distillation stands as the cornerstone unit operation in industrial sectors, vital for purifying desired products efficiently. Despite its importance, these units are notorious energy consumers, accounting for approximately 3% of the world's total energy consumption and consuming about 50% of the energy used in the chemical and petrochemical industries. However, their efficiency has historically been a challenge. Over recent decades, extensive research has focused on enhancing distillation column designs. Innovations include split-wall columns, thermally coupled configurations, thermodynamically equivalent setups, and proposals for intensified operations integrating reactive stages within columns.

Many studies have aimed at optimizing both the configuration and operational parameters of distillation columns. However, achieving optimal efficiency hinges significantly on tray design (tray hydrodynamics) and operational conditions, which dictate the flow regime within the tray. While traditional methods such as MESH equations and sequential simulators have been instrumental in studying these designs, Computational Fluid Dynamics (CFD) has received less attention due to its computational complexity. However, CFD studies are highly relevant for the industrial design of distillation columns because they provide a detailed understanding of the fluid flow, heat transfer, and mass transfer processes within the column. This detailed insight allows for more accurate predictions and

optimizations of the column's performance, leading to more efficient and cost-effective designs.

CFD can simulate complex phenomena such as vapor—liquid interactions, flow maldistribution, and pressure drop, which are challenging to capture with traditional methods, thus offering a significant advantage in enhancing the design and operation of distillation columns. For instance, CFD allows engineers to visualize the flow patterns and identify areas where inefficiencies or potential problems such as flooding or weeping might occur. This visualization capability is crucial for designing trays and packing that maximize contact between phases and improve mass transfer efficiency.

Moreover, CFD can be used to study the impact of different operational conditions, such as varying feed rates or compositions, on the performance of the column. This ability to conduct virtual experiments reduces the need for costly and time-consuming physical testing. Additionally, CFD can aid in scaling up processes from pilot plants to full-scale industrial operations by providing insights that ensure the scalability of the design without compromising performance.

Received: September 4, 2024 Revised: November 25, 2024 Accepted: November 28, 2024 Published: December 7, 2024





Furthermore, advancements in computational power and techniques have made CFD more accessible and practical for industrial applications. High-performance computing and parallel processing enable the handling of the large, complex simulations required for accurate modeling of distillation columns. Consequently, CFD is becoming an indispensable tool in the arsenal of chemical engineers, complementing traditional methods and pushing the boundaries of what is possible in the design and optimization of distillation processes.

Numerical analysis plays a pivotal role in evaluating column efficiency by simulating changes in column design or geometry. CFD simulations provide insights into flow dynamics within distillation trays, capturing essential transport phenomena in equilibrium stages. Results typically include detailed velocity fields and turbulence characteristics across the vessel, offering valuable insights into flow physics despite the complexities involved.

Researchers have tackled various aspects of tray designs, often focusing on industrial-scale trays <sup>9-15</sup> with specific geometries and configurations. Some investigations have explored changes in tray geometries, such as altering free areas, <sup>16</sup> adopting orthogonal hole patterns, <sup>17-19</sup> incorporating inclined perforations, <sup>20</sup> or studying the effects of hole and bubble sizes. <sup>17</sup> Different tray types, including sieve trays, <sup>12,13,21-23</sup> bubble cap trays, <sup>24</sup> and conical cap trays, <sup>25</sup> have been scrutinized for their hydrodynamic performance, examining parameters like velocity distribution, clear liquid height, and liquid volumetric fractions.

Due to the computational demands of solving millions of partial differential equations governing heat, momentum, and mass transfer, studies have employed strategies like transient flow models,<sup>22</sup> symmetry axis analyses,<sup>26</sup> and localized plate region assessments<sup>17,27</sup> to manage computational costs. However, these approaches may not fully capture the entire fluid behavior, particularly around complex regions like downcomers,<sup>3,28</sup> limiting their applicability to specific scenarios studied.

CFD methodologies typically employ either Eulerian or Lagrangian approaches. Eulerian methods discretize media using a mesh, facilitating spatial averaging at fluid interfaces. Popular examples include finite volume and finite element methods, chosen for their ability to model hydrodynamics, mass transfer, and momentum within distillation columns. <sup>29–32</sup> Challenges include interface modeling, convergence issues, and selecting appropriate turbulence models for simulating turbulent flows.

In contrast, Lagrangian methods offer detailed insights into interface phenomena by discretizing continuous media into nonmeshed points. Smoothed Particle Hydrodynamics (SPH) is an emerging Lagrangian method adept at representing discontinuous media and intricate geometries using particles, avoiding the constraints of a mesh. SPH has proven versatile in modeling diverse scenarios such as microbial growth, 33 ocean wave dynamics, 34 and astrophysical phenomena, 35 highlighting its applicability and robustness.

Eulerian methods, which rely on central processing units (CPUs), face significant increases in computational complexity as the number of cells increases. This is due to the inherent limitations of CPUs in handling large-scale, parallel computations efficiently. In contrast, the Smoothed Particle Hydrodynamics (SPH) method employed in our study reduces computational costs by leveraging parallel computation on GPUs. GPUs are particularly well-suited for SPH simulations due to their ability to handle a large number of particles

simultaneously, thus providing a significant performance advantage.

The SPH method offers several key advantages over traditional Eulerian methods:

- Parallel Computation: SPH leverages the parallel processing power of GPUs, allowing for efficient handling of large particle counts.
- Scalability: The method scales well with increasing particle numbers, making it suitable for high-resolution simulations.
- Flexibility: SPH is inherently adaptable to complex geometries and boundary conditions, which is beneficial for accurately modeling real-world systems.

For the detailed study of liquid-vapor equilibrium dynamics in a sieve tray within a distillation column, Lagrangian methods, particularly Smoothed Particle Hydrodynamics (SPH), present the preferred computational approach. Lagrangian methods offer distinct advantages in modeling intricate geometries and multiphase flows without the constraints of a structured mesh. This flexibility is crucial for accurately capturing the complex fluid dynamics, including bubble patterns and liquid-vapor interfaces, essential for understanding tray performance in mass and heat transfer. Unlike Eulerian methods, which use a fixed or mobile spatial discretization and the mathematical model is solved in the central processing unit (CPU). Lagrangian methods excel in simulating scenarios with varying fluid behavior and geometry, such as those encountered in distillation tray simulations. Their ability to track individual fluid particles enhances the precision of modeling turbulent and nonuniform flows, making them ideal for optimizing distillation column efficiency through detailed hydrodynamic analysis. In addition, the SPH method is coded in the Compute Unified Device Architecture (CUDA) language, so it has the ability to use the Graphics Processing Unit (GPU) cards to solve the mathematical model in parallel on the GPU cores and significantly reduce the computational cost. On the other hand, due to the nature of the method, it is not necessary to couple turbulence models to model the behavior of fluids, which allows to significantly increase the number of particles and refine the solution.<sup>36</sup>

Due to the complexity of modeling the multiphase flow behavior that occurs within an equilibrium stage of a distillation column, tray design is based on empirical knowledge.<sup>37</sup> The main reason for this is the limited understanding of the mass, heat and momentum transfer phenomena within the plate. Therefore, knowledge of these phenomena will allow more efficient tray to be designed and flow patterns to be related to design parameters such as gas and liquid loads, column diameter, weir height, weir length, diameter of holes, fractional hole area, active bubbling area, downcomer area. and physicochemical properties of the system. An alternative is the analysis of the hydrodynamics within a tray, as it allows prediction of the flow regime prevailing on the tray, liquid hold-up, clear liquid height, froth density, interfacial area, pressure drop, liquid entrainment, gas and liquid phase residence time distributions, and mass transfer coefficients in both liquid phases.<sup>23</sup>

In this study, we propose a detailed numerical simulation using the Smoothed Particle Hydrodynamics (SPH) method to analyze the hydrodynamics and heat transfer in the liquid—vapor equilibrium stage of a sieve tray within a distillation column. This simulation facilitates the description of flow patterns, velocity, pressure, and temperature profiles on the sieve tray.

Heat transfer coefficients and physicochemical properties of the system are estimated through the rigorous solution of the MESH equations in the AspenOne simulator. The simulation employs periodic temperature conditions to accurately represent the equilibrium stage, utilizing parameters derived from an AspenOne simulation of benzene-toluene separation. This approach aims to provide comprehensive insights into tray performance and optimize distillation column efficiency under varying operating conditions and tray geometries.

The analysis offers a deep understanding of the interaction between liquid and vapor phases, the effect of geometry by varying the percentage of free area, and its relationship to the flow regime, flow patterns, velocity fields, and temperature fields over time within the sieve tray. The goal is to provide a detailed view of the dynamic behavior of sieve trays, enabling the optimization of distillation column design and operation to enhance separation efficiency and energy efficiency. Furthermore, the study evaluates conditions affecting tray performance, including variations in phase distribution, mass and heat transfer characteristics, and the impact of geometric modifications on the overall performance of the column.

This study is highly relevant at an industrial level because distillation is one of the most widely used separation processes in the chemical and petrochemical industries. The efficiency and effectiveness of distillation columns directly impact the operational costs, energy consumption, and product quality. By providing a detailed and accurate simulation of the liquidvapor equilibrium stage, this research can lead to significant improvements in the design and operation of distillation columns. Optimizing tray performance and understanding the intricate interactions within the column can result in reduced energy usage, lower operational costs, and enhanced process efficiency, which are crucial factors for maintaining competitiveness and sustainability in industrial processes.

### 2. SPH METHOD

The Smoothed Particle Hydrodynamics (SPH) method is a numerical and Lagrangian technique for solving differential equations. The SPH method decomposes the physical domain of the material under consideration into smaller elements called particles. Each particle represents a portion of the material and interacts with other particles according to the governing equations of fluid dynamics.

SPH is a Lagrangian method, meaning it follows individual particles as they move through space and time. This approach contrasts with Eulerian methods, which observe changes at fixed points in space. Each particle carries properties such as mass, position, velocity, and other relevant physical quantities, which evolve according to the governing equations. Particles interact with one another through a kernel function, which smooths the influence of a particle over a finite region. This smoothing process helps to avoid singularities and provides a continuous representation of field quantities. The choice of kernel function and its parameters significantly impacts the accuracy and stability of the SPH method.

The primary equations used in SPH are derived from fluid dynamics, including the Navier-Stokes equations for momentum conservation and the continuity equation for mass conservation. These equations are discretized in the SPH framework using particles and kernel functions, allowing for the simulation of complex fluid behavior. The SPH method was independently developed in 1977 by two groups of researchers. Gingold and Monaghan,<sup>38</sup> as well as Lucy,<sup>39</sup> introduced the

method while studying the collapse of stellar clouds. In their work, each particle represented a volume segment of the collapsing gas, interacting with others through the equations of fluid dynamics. This innovative approach allowed for the simulation of astrophysical phenomena that were difficult to model using traditional grid-based methods.

SPH has been widely adopted in various fields, including astrophysics, engineering, and geophysics, due to its flexibility and ability to handle complex, dynamic systems with large deformations and free surfaces. Its applications range from simulating star formation and galaxy dynamics to modeling fluid flow in engineering systems and natural disasters such as landslides and tsunamis. The mesh-free nature of SPH makes it suitable for problems with large deformations and complex geometries. The method's adaptive resolution allows for higher resolution in regions of interest, improving accuracy. Additionally, SPH can easily handle problems with moving boundaries and free surfaces.

However, SPH also presents challenges. The method can be computationally expensive due to the need to evaluate interactions between many particles. Implementing accurate and efficient boundary conditions can be challenging in SPH simulations. Ensuring stability and accuracy requires careful selection of kernel functions and numerical parameters. Despite this challenges, 40-42 the SPH method continues to evolve, with ongoing research aimed at improving its accuracy, efficiency, and applicability to a broader range of problems.

**2.1. Interpolation.** The interpolation performed by SPH for calculating physical magnitudes such as temperature, density, elongation, stress, among others, is based on the characteristic definition of the Dirac delta.

$$f(x) = \int_{\Omega'} f(x')\delta(x' - x) d\Omega'$$
(1)

SPH relies on this property of the Dirac delta to transform the variables of the function f from x to x' within a volume  $\Omega'$  to propagate the properties of one point in space to others. However, computationally, the definition given in eq 1 presents an inconvenience, which can be observed in the alternative definition of the delta.

$$\delta(x' - x) = \begin{cases} \infty & \text{if } x' = x \\ 0 & \text{if } x' \neq x \end{cases}$$
 (2)

It shows that the delta has a maximum at x' = x with infinite height and infinitesimal width. Computationally, eq 2 cannot be recreated due to resolution and floating-point problems. Therefore, the idea of SPH is to smooth the Dirac delta with a function called the smoothing function or Kernel (W), which approximates the delta to a finite value within a noninfinitesimal circular domain of radius h, called the smoothing length. This Kernel depends on the same variables as the delta, W = W(x' x), and its shape should resemble a bell curve. The definition of the interpolation of any sufficiently smooth function f(x) with the Kernel becomes.

$$f(x) \cong \int_{\Omega'} f(x')\delta(x'-x)d\Omega'$$
 (3)

However, in performing this approximation, the equality achieved in (1) is lost, and the right-hand side of (3) becomes the SPH approximation or interpolation (denoted within angular brackets) of the function f.

$$\langle f(x,h) \rangle \cong \int_{\Omega'} f(x')W(x'-x)d\Omega'$$
 (4)

Therefore, the closer the kernel is to the delta, the better the SPH interpolation will approximate the true function,  $\langle f(x) \rangle \rightarrow$ f(x). To achieve a good convergence of the function f(x) while considering computational limitations, the smoothing function must have the following properties: It must be positive to prevent the sign of the function from changing due to the values of the kernel; it must be symmetric, it should preserve parity with respect to the coordinates and not depend on angles; it must be a monotonically decreasing function, this ensures, along with the previous conditions, that it has a single maximum located at the center of the domain; it must converge to the Dirac delta for small values of h; it must be normalized, this ensures nondivergence; it must have compact support, the kernel and its derivatives should monotonically decrease to zero at the edges of the domain, within a finite distance greater than kh, where k is a constant dependent on the kernel. In general, for a function to serve as a Kernel, it must be nonzero, smooth, and have support in its derivatives.

$$W(|x' - x|, h) = 0 \dots \frac{d^n W}{dx^n} (|x - x'|, h) = 0$$
if  $|x - x'| > kh$  (5)

Some examples of Kernels used in the literature are shown below:

Cubic B-Spline: This is the most extensively used Kernel in the literature 43 due to its resemblance to the Gaussian function and its computational efficiency as a cubic polynomial. It is also recommended by Monaghan in his review articles from 1992 44,45 and 2005, 46 and it was first used in the 1985 paper by Monaghan and Lattanzio. 47

$$W(q, h) = \frac{\lambda_d}{\pi h^d} \times \begin{cases} \frac{2}{3} - q^2 + \frac{1}{2}q^3 & q \le 1\\ \frac{1}{6}(2 - q)^3 & 1 \le q \le 2\\ 0 & q \ge 2 \end{cases}$$
 (6)

where  $\lambda_1 = \pi$ ,  $\lambda_2 = \frac{15}{7}$ ,  $\lambda_3 = \frac{3}{2}$ .

Wendland C4: There are various types of Wendland functions with different orders demonstrated by the author. <sup>48</sup> The one shown and used in this work is the C4.

$$W(q, h) = \frac{\lambda_d}{\pi h^d} \times \begin{cases} (1 - q)^6 \left( 1 + 6q + \frac{32}{3} q^2 \right) & q \ge 1\\ 0 & q \ge 1 \end{cases}$$
 (7)

where  $\lambda_2 = 9$ ,  $\lambda_3 = \frac{4953}{32}$ .

The spatial derivative of a physical quantity can be calculated in SPH directly from the definition (2.3).

$$\langle \frac{\mathrm{d}f}{\mathrm{d}x}(x) \rangle = \int_{\Omega'} \frac{\mathrm{d}f}{\mathrm{d}x'}(x') W(|x'-x|, h) \mathrm{d}\Omega'$$
(8)

$$\langle \frac{\mathrm{d}f}{\mathrm{d}x}(x) \rangle = f(x')W(|x'-x|, h)_{\Gamma'} - \int_{\Omega'} f(x') \frac{\partial W}{\partial x'}(|x'-x|, h) \mathrm{d}\Omega'$$
(9)

let  $\Gamma$  be the surface of the system; furthermore, integration by parts has been used. The kernel must have compact support, so it is zero on the surface and, moreover, it is symmetric, so its derivative is antisymmetric.

$$\frac{\mathrm{d}W}{\mathrm{d}x'} = -\frac{\mathrm{d}W}{\mathrm{d}x} \tag{10}$$

$$\langle \frac{\mathrm{d}f}{\mathrm{d}x}(x)\rangle = \int_{\Omega'} f(x') \frac{\partial W}{\partial x'} (|x' - x|, h) \mathrm{d}\Omega'$$
(11)

SPH allows the derivatives of a quantity to be easily defined from the derivative of the kernel, which, being known, can be calculated even before defining the system.

**2.2. SPH Formalism Used for Fluid Dynamics Equations.** This section describes the equations governing fluid dynamics in SPH form, which are derived from the continuous form of each equation using the equations shown in the interpolation Section 2.1. The eq 12 presents the continuity equation described in Lagrangian form.

$$\frac{\mathrm{d}\rho}{\mathrm{d}t} = -\rho \nabla \bullet \mathbf{v} \tag{12}$$

where  $\rho$  is density, t is time,  $\mathbf{v}$  is de velocity vector and  $\nabla$  is the nabla operator.

Considering the continuity equation for one particle a

$$\frac{\mathrm{d}\rho_a}{\mathrm{d}t} = -\rho_a (\nabla \bullet \mathbf{v})_a \tag{13}$$

Using the eq 11 to evaluate the gradient of the eq 13

$$\frac{\mathrm{d}\rho_a}{\mathrm{d}t} = -\rho_a \sum_{b=1}^n m_b \frac{\mathbf{v}_b}{\rho_b} \bullet \nabla_a W_{ab} \tag{14}$$

where the subscript b refers to the neighbor particles inside the kernel and m is the mass of the particle.

The eq 14 is the continuity equation in the SPH formalism. Using identities, it is possible to obtain different discrete equations, as example if

$$-\rho_a(\nabla \bullet \mathbf{v})_a = -\nabla \bullet (\rho \mathbf{v})_a + \mathbf{v}_a \bullet \nabla \rho_a \tag{15}$$

it is possible obtain the next discrete equation

$$\frac{\mathrm{d}\rho_a}{\mathrm{d}t} = -\nabla \bullet (\rho \mathbf{v})_a + \mathbf{v}_a \bullet \nabla \rho_a = \sum_{b=1}^N m_b (\mathbf{v}_a - \mathbf{v}_b) \bullet \nabla_a W_{ab}$$
(16)

considering now the momentum equation in the way

$$\frac{\mathrm{d}\mathbf{v}}{\mathrm{d}t} = -\nabla \left(\frac{P}{\rho}\right) - \frac{P}{\rho^2} \nabla \rho \tag{17}$$

using again the eq 13 to evaluate the gradient, we can obtain the momentum equation in a discrete SPH form

$$\frac{\mathrm{d}\mathbf{v}}{\mathrm{d}t} = -\sum_{b=1}^{N} m_b \frac{P_b}{\rho_b^2} \nabla_a W_{ab} - \frac{P_a}{\rho_a^2} \sum_{b=1}^{N} m_b \frac{\rho_b}{\rho_b} \nabla_a W_{ab} 
= -\sum_{b=1}^{N} m_b \left( \frac{P_b}{\rho_b^2} + \frac{P_a}{\rho_a^2} \right) \nabla_a W_{ab}$$
(18)

**2.3. DualSPhysics Model.** Currently, three branches of the SPH method have been developed: the standard model (Monaghan 1992), the quasiincompressible model, 49,50 and the incompressible model. 51 The model used in this work is

based on the quasi-incompressible model, which utilizes the DualSPHysics code in its online version and upon which it was implemented. This section presents the complete SPH model reported by Aragón et al.,52 which is used to simulate the L-V equilibrium in a stage of a distillation column.

The change of density, momentum and temperature for each phase within the stage is calculated using the eqs 19-21 which are solved using an original modified version of the open-source code DualSPHysics.5

$$\frac{\mathrm{d}\rho}{\mathrm{d}t} = -\rho \nabla \bullet \mathbf{v} \tag{19}$$

$$\frac{\mathrm{d}\mathbf{v}}{\mathrm{d}t} = -\frac{1}{\rho}\nabla p + \nu\nabla^2\mathbf{v} + \mathbf{F} \tag{20}$$

$$\frac{\mathrm{d}T}{\mathrm{d}t} = \frac{1}{\rho C_{\mathrm{p}}} \nabla \bullet (k \nabla T) \tag{21}$$

where p is pressure,  $C_p$  is the heat capacity, T is temperature,  $\nu$  is the viscosity and k is the constant conductivity. Equations 19 and 20 are closed by a equation state with the form

$$p = B \left[ \left( \frac{\rho}{\rho_r} \right)^{\gamma} - 1 \right] \tag{22}$$

where  $B = c_0^2 \rho_r / \gamma$ ,  $\rho_r$  is a reference density,  $\gamma = 7$  for liquids and  $\gamma$ = 1.4 for gases, and  $c_0$  is a numerical speed of sound which must be at least 10 times higher than the maximum velocity of the fluid in the system to ensure a maximum density fluctuation of 1% satisfying the compressibility condition. 44,46

The density variation by particle is calculated according to the eq 23 which is convenient in cases with density discontinuities, as is the cases of multiphase flow (L-V).

$$\frac{\mathrm{d}\rho_a}{\mathrm{d}t} = \sum_{b=1}^N m_b (\mathbf{v}_a - \mathbf{v}_b) \bullet \nabla_a W_{ab}$$
(23)

The momentum eq 20 is solved using the following

$$\frac{\mathrm{d}\mathbf{v}}{\mathrm{d}t} = -\sum_{b=1}^{N} m_b \left(\frac{p_a + p_b}{\rho_a \rho_b}\right) \nabla_a W_{ab} + 2\nu \sum_{b=1}^{N} m_b \frac{\mathbf{v}_{ab} \mathbf{x}_{ab} \bullet \nabla_a W_{ab}}{\widehat{\rho}_{ab} |\mathbf{x}_{ab}|^2 + \varepsilon^2}$$

Where  $\mathbf{v}_{ab} = \frac{\mathbf{v}_a + \mathbf{v}_b}{2}$ ,  $\hat{\rho}_{ab} = \frac{\rho_a + \rho_b}{2}$ ,  $\mathbf{x}_{ab} = \mathbf{x}_a - \mathbf{x}_b$  and  $\varepsilon^2 = 0.01 \ h^2$  is a small correction factor used to avoid singularities when  $|\mathbf{x}_{ab}|^2 \ll 1$ .

According to [37] the eq 21 is given in the SPH form as

$$\frac{\mathrm{d}T_a}{\mathrm{d}t} = \frac{2k}{\rho_a c_p} \sum_{b=1}^N \frac{m_b}{\rho_b} \frac{T_{ab} \mathbf{x}_{ab} \bullet \nabla_a W_{ab}}{|\mathbf{x}_{ab}|^2 + \varepsilon^2}$$
(25)

where  $T_{ab} = T_a - T_b$ . Using this form the continuous heat flux across the material is guaranteed.

The motion of the particles in a SPH frame is calculated according to

$$\frac{\mathrm{d}\mathbf{x}_a}{\mathrm{d}t} = \mathbf{v}_a \tag{26}$$

which must be solved simultaneously with eqs 23-25.

The eqs 23-25 can be integrated in time using different algorithms, 54 in this work is used the Verlet algorithm provided

by DualSPHysics and described in eqs 27-30 where the properties of the particle a are advanced from time  $t^n$  to  $t^{n+1} = tn$ 

$$\rho_a^{n+1} = \rho_a^{n-1} + 2\Delta t \left(\frac{\mathrm{d}\rho_a}{\mathrm{d}t}\right)^n \tag{27}$$

$$\mathbf{v}_{a}^{n+1} = \mathbf{v}_{a}^{n-1} + 2\Delta t \left(\frac{\mathrm{d}\mathbf{v}_{a}}{\mathrm{d}t}\right)^{n} \tag{28}$$

$$\mathbf{x}_{a}^{n+1} = \mathbf{x}_{a}^{n} + \Delta t \mathbf{v}_{a}^{n} + 0.5 \Delta t^{2} \left(\frac{\mathrm{d}\mathbf{x}_{a}}{\mathrm{d}t}\right)^{n}$$
(29)

$$T_a^{n+1} = T_a^{n-1} + 2\Delta t \left(\frac{\mathrm{d}T_a}{\mathrm{d}t}\right)^n \tag{30}$$

Numerical coupling of the discrete SPH equations is ensured during the evolution by alternating the above steps by eqs 31-34

$$\rho_a^{n+1} = \rho_a^n + 2\Delta t \left(\frac{\mathrm{d}\rho_a}{\mathrm{d}t}\right)^n \tag{31}$$

$$\mathbf{v}_{a}^{n+1} = \mathbf{v}_{a}^{n} + 2\Delta t \left(\frac{\mathrm{d}\mathbf{v}_{a}}{\mathrm{d}t}\right)^{n} \tag{32}$$

$$\mathbf{x}_a^{n+1} = \mathbf{x}_a^n + \Delta t \mathbf{v}_a^n + 0.5 \Delta t^2 \left(\frac{\mathrm{d}\mathbf{x}_a}{\mathrm{d}t}\right)^n \tag{33}$$

$$T_a^{n+1} = T_a^n + 2\Delta t \left(\frac{\mathrm{d}T_a}{\mathrm{d}t}\right)^n \tag{34}$$

The time step  $\Delta t$  is calculated according to the minimum value between the following steps, eqs 35-39.

$$\Delta t_f = \min_a \left( h \left| d\mathbf{v}_a / dt \right|^{-1} \right)^{1/2} \tag{35}$$

$$\Delta t_{v,a} = \max_{b} |h \mathbf{x}_{ab} \bullet \mathbf{v}_{ab} / (\mathbf{x}_{ab} \bullet \mathbf{x}_{ab} + \varepsilon^{2})|$$
(36)

$$\Delta t_{cv} = \min_{a} [h(c_0 + \Delta t_{v,a})^{-1}]$$
(37)

$$\Delta t_e = \min_a (0.1 \rho_a c_p h^2 / k) \tag{38}$$

$$\Delta t = \min(\Delta t_f, \, \Delta t_{cv}, \, \Delta t_e) \tag{39}$$

The surface tension force *F* is modeled under the concept of the interfacial tension of the water-oil system. In this work, we used the attraction and repulsion model proposed by Tartakovsky and Meakin<sup>55</sup> expressed in the eq 40

$$F = \sum_{b} F_{ab} = \begin{cases} S_{ab} \cos\left(\frac{1.5\pi}{3}|r_b - r_a|\right), |r_b - r_a| \le h \\ 0, |r_b - r_a| > h \end{cases}$$
(40)

where  $S_{ab}$  is the magnitude of the force between the particles a

The magnitude of the force  $(S_{ab})$  must be greater in the interaction between particles of the same phase compared to the force when interacting particles of different phases, so  $S_{a1}S_{b1} \gg$  $S_{a1}S_{b2}$  and the value of force in the same phase can be calculated as function of the variable smoothing length (h) and the real surface tension between fluids ( $\sigma$ ) using the eq 41

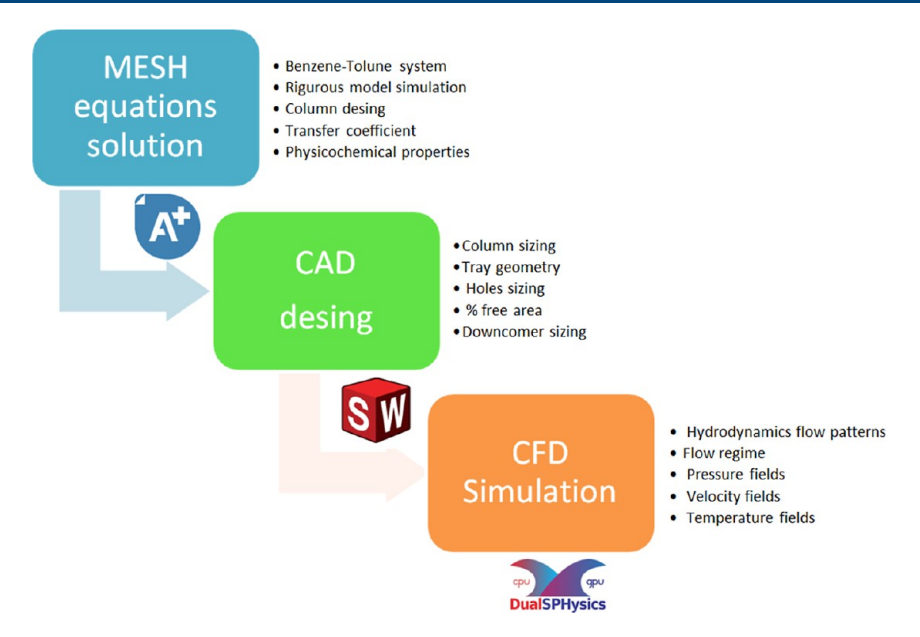


Figure 1. Methodology for the numerical simulation of the hydrodynamics and heat transfer within sieve tray.

$$S_1 S_1 = S_2 S_2 = \frac{1}{2} n^{-2} \left(\frac{h}{3}\right)^{-5} \frac{\sigma}{\lambda} \tag{41}$$

#### 3. METHODOLOGY

In this paper, we propose a comprehensive methodology for applying the novel Lagrangian approach to numerical analysis within the liquid-vapor (L-V) equilibrium stage of a distillation column using the Smoothed Particle Hydrodynamics (SPH) method. This methodology is structured into three detailed steps: solving the MESH equations, creating a CAD model, and performing a CFD simulation (Figure 1).

- 1 MESH Equation Solution: The first step involves simulating the distillation column through rigorous computational methods by solving the MESH equations (Mass, Energy, Summation, and Heat balance equations) using AspenOne software. This simulation is crucial for obtaining the necessary operational parameters and properties of the system, including the column diameter, temperature and pressure profiles, heat transfer coefficients, and the physicochemical properties of the working fluids. These parameters form the foundation for the subsequent steps, ensuring that the system is well-defined and accurately represented.
- 2 CAD Modeling: In the second step, the physical dimensions of the column and its sieve trays are determined based on the data acquired from the MESH equation solutions. A detailed three-dimensional computer-aided design (CAD) model of the distillation column, including three sieve trays with varying free area percentages, is created using SolidWorks. This step involves precise geometric modeling to ensure that the physical structure aligns with the operational specifications and constraints identified in the first step. The CAD model serves as a critical intermediary, translating theoretical and computational results into a tangible design that can be used for further analysis and simulation.
- 3 CFD Simulation: The final step involves performing a computational fluid dynamics (CFD) simulation to analyze the hydrodynamics and heat transfer within the

distillation column. Using the DualSPHysics software, which employs the SPH method, we simulate the fluid flow and thermal behavior within the column. This simulation focuses on determining the flow regime, hydrodynamic flow patterns, and the velocity, pressure, and temperature fields within an equilibrium stage of the column. The initial conditions and parameters for this simulation, such as heat transfer coefficients and physicochemical properties, are derived from the data obtained in the first step. This ensures continuity and accuracy across the methodology. The CFD simulation provides detailed insights into the internal processes of the column, which are essential for optimizing design and operational parameters.

This methodology not only provides a robust framework for the numerical analysis of distillation columns but also integrates advanced computational techniques to enhance the accuracy and reliability of the results. By combining rigorous equationsolving methods, precise CAD modeling, and sophisticated CFD simulations, this approach offers a comprehensive toolset for the detailed analysis and optimization of distillation processes.

**3.1. Case Study.** A benzene-toluene mixture was selected for this analysis due to its significant industrial applications and the fundamental role both compounds play in various manufacturing processes. Toluene is utilized in the production of phenol, polyurethane, benzyl alcohol, and benzoic acid. It is also converted into benzene via hydrodisalkylation. Toluene is sourced from olefin plants, crude oil, and coke production processes, and can be separated from reforming streams by heating, followed by purification through solvent extraction or fractional distillation. 56 Benzene, a precursor to polymers such as polystyrene, resins, and nylon, is essential in the manufacture of styrene, cumene, and cyclohexane. 57 It is a natural component of crude oil. The separation of benzene and toluene is relatively straightforward due to the notable difference in their boiling points and their slight positive deviation from ideal solution behavior.<sup>58</sup> For this study, an equimolar mixture was chosen, reflecting the equal importance of both compounds in the chemical, petrochemical, and pharmaceutical industries. The

choice of an equimolar mixture simplifies the analysis and allows for a balanced assessment of the distillation process's efficiency. Additionally, the benzene-toluene mixture was selected as a representative mixture for the separation of aromatics. Because the aromatic family has densities and viscosities are similar to benzene. <sup>59</sup>

A sieve tray distillation column was selected for this process due to its widespread industrial use and effectiveness in handling mixtures with varying properties. Sieve trays offer several advantages:

- Efficiency: They provide good vapor—liquid contact, which is crucial for the efficient separation of benzene and toluene.
- Versatility: Sieve trays are suitable for a wide range of operating conditions, making them ideal for the varying properties of benzene-toluene mixtures.
- Maintenance: They are relatively easy to maintain and clean compared to other tray types, reducing downtime and operational costs.
- Scalability: Sieve trays can be easily scaled up for larger production volumes, accommodating industrial demands.

The distillation column design was conducted using AspenOne software, ensuring it met the criteria for a total condenser with a cooling water temperature of 120 °F. The RadFrac model within AspenOne, known for its robust and precise approach, was utilized, leveraging rigorous methods founded on the MESH (Mass, Energy, Summation, and Heat) equations. The thermodynamic model selected to represent the liquid—vapor equilibrium was the NonRandom Two-Liquid (NRTL) model, which is well-suited for handling the complexities of nonideal mixtures. <sup>60</sup> The NRTL model can be used to calculate the VLE and LLE and is recommended for nonideal mixtures. <sup>61,62</sup>

The preliminary design phase employed simplified methods to ensure that the condenser would effectively utilize cooling water at the specified temperature. Following this, a detailed and rigorous design of the sieve tray distillation column was undertaken using the RadFrac module in AspenOne. This comprehensive simulation was instrumental in optimizing the column design via a sophisticated stochastic algorithm, complemented by a constraint-handling technique. <sup>60</sup>

The primary objective of the optimization was to minimize the heat duty required by the distillation process. Key design variables subject to optimization included the total number of stages in the column, the specific stage where the feed is introduced, and the reflux ratio. The constraints for the optimization problem were stringent, requiring 98% recovery and 98% purity for each component in the distillation process.

The optimization algorithm employed was the Boltzmann Univariate Marginal Distribution Algorithm (BUMDA). The BUMDA algorithm has been used to solve highly nonlinear, nonconvex problems subject to design constraints, showing its robustness to the search for optimal designs, as in the case of HiDiC column optimization. He belongs to the category of population distribution algorithms (EDAs). These algorithms aim to find the optimum by proposing a set of candidate solutions. They generate new individuals from a selected subset that improves the previous population from its probability distribution. In EDA's, the selection method used is truncation, which is performed by ordering the population. The best fraction of the population is selected to generate the individuals of the next population. This is done by calculating the mean and

variance of each dimension (design variable). The BUMDA algorithm was selected for its ability to leave local optima, since the search distribution reflects the fitness values of the selected set through the Boltzmann distribution. That is, the better the fitness value of an individual, the higher the probability of sampling in that region.<sup>65</sup>

Another important feature of the BUMDA algorithm is that the mode of the Boltzmann distribution coincides with the optimum of the objective function. This ensures that the search proceeds in the direction of the optimum, despite the possible existence of clusters of points in each region where the optimum is not found. The features described above allow a significant reduction of the computational cost. The parameters of the BUMDA algorithm are: the number of individuals per generation and the truncation of the population, obtained through a tuning process.

The first generation of the BUMDA algorithm is randomly obtained by the lower and upper bounds of each variable. These individuals are evaluated with respect to the objective function. Only the best 30% of individuals from generation G are selected to determine the mean and variance used to generate the next population G+1. This process is iterated until the stopping criterion is reached. In this case, the number of function evaluations is established as the stopping criterion. This criterion is the most commonly used in evolutionary algorithm literature.  $^{66}$ 

This advanced algorithm operates with a population of 60 individuals per generation. During each generation, the parameters of a normal distribution are determined and updated. The selection criterion by truncation corresponds to one-third of the population; this value is recommended to have an adequate selection pressure for the problem. The optimization process reaches its conclusion when the variance value remains below  $1\times10^{-6}$  for three consecutive generations, ensuring convergence to a stable solution. In this specific case study, the stop criterion was achieved after approximately 3000 function evaluations.

The optimization process was crucial in refining the column's operating parameters to achieve the desired separation efficiency, recovery, and purity levels. The optimal design determined through this process includes 14 stages in total, with the feed stream entering at stage 6. The optimal reflux ratio was found to be 3.179. The heat duty required for this configuration is 55.77 kW, and the column diameter is specified as 0.208 m. Detailed profiles of concentration, temperature, pressure, and flow rates across the stages are provided in Tables S1 and S2 in the Supporting Information.

The feed stream was introduced into the column as a saturated liquid at stage 6. This specific feed condition directs the liquid flow toward the rectification zone of the column, making the analysis of the postfeed stages crucial to understanding the internal dynamics of the column. Therefore, stages 7, 8, and 9 were selected for detailed numerical analysis. This selection is critical because the MESH equations necessitate knowledge of the behavior of adjacent stages (N-1 and N+1) to accurately compute the liquid—vapor equilibrium at any given stage (stage N in this study being stage 8).

By focusing on stages 7, 8, and 9, the study ensures a comprehensive understanding of the interactions and equilibrium processes occurring in the column postfeed stage. The behavior of these stages significantly influences the overall separation efficiency and the quality of the distilled products.

The insights gained from this analysis are vital for fine-tuning the column's operation and achieving optimal performance.

Furthermore, the rigorous approach adopted in this study, encompassing both preliminary and detailed design phases, along with advanced optimization techniques, underscores the importance of a thorough and meticulous design process in achieving high-efficiency distillation operations. The successful application of AspenOne software, combined with the NRTL model and the BUMDA optimization algorithm, exemplifies a robust framework for designing and optimizing distillation columns in complex chemical processes.

The outcomes of this study not only highlight the technical feasibility of the designed distillation column but also provide a solid foundation for its practical implementation in industrial settings. The detailed profiles and the optimal design parameters serve as valuable references for engineers and practitioners in the field, facilitating informed decision-making and enhancing the efficiency of distillation operations.

3.1.1. Simulation and Results. The rigorous simulation of the distillation column was conducted adhering to detailed specifications and operational conditions. The comprehensive

Table 1. Results of the Rigorous Simulation of the Distillation Column in AspeOne

| param  | eter             | liquid                  | vapor                |
|--|------------------|-------------------------|----------------------|
| surface tension                              |                  | 0.018 N/m               |                      |
| density (kg/m³)                              |                  | 783.8023                | 4.0206               |
| viscosity (Ns/m²)                            |                  | $2.5 \times 10^{-4}$    | $9.5 \times 10^{-6}$ |
| volume flow $(m^3/s)$                        |                  | 0.00023                 | 0.0379               |
| column diameter (m)                          |                  | 0.208                   |                      |
| coefficient of thermal diffusivity $(m^2/s)$ |                  | $7.9247 \times 10^{-8}$ |                      |
| stage  | temperature (°C) | pressi                  | are $(N/m^2)$        |

| stage | temperature (°C) |         | pressure (N/m²) |  |
|-------|------------------|---------|-----------------|--|
|       | liquid           | vapor   |                 |  |
| 7     | 101.186          | 105.506 | 133,174.889     |  |
| 8     | 105.506          | 110.517 | 138,478.549     |  |
| 9     | 110.517          | 115.610 | 143,782.208     |  |
|       |                  |         |                 |  |

results, summarized in Table 1, encompass the following critical aspects:

- Column Diameter: The diameter was calculated based on the vapor and liquid traffic within the column, ensuring optimal flow dynamics and efficient phase separation.
- Temperature and Pressure Tray Study: This analysis is crucial for understanding the thermal hydrodynamics across different trays in the column. It provides insights into the temperature and pressure profiles, which are essential for the accurate design and operation of the distillation process.
- Coefficient of Thermal Diffusivity: This parameter is vital
  for the heat transfer efficiency from tray to tray. Accurate
  knowledge of thermal diffusivity helps in optimizing the
  thermal gradients and improving the overall heat
  integration within the column.
- Physicochemical Properties: The physicochemical properties of the components, such as boiling points, vapor pressures, and specific heats, play a significant role in the separation process. These properties influence the vapor—liquid equilibrium and are critical inputs for the simulation and design process.

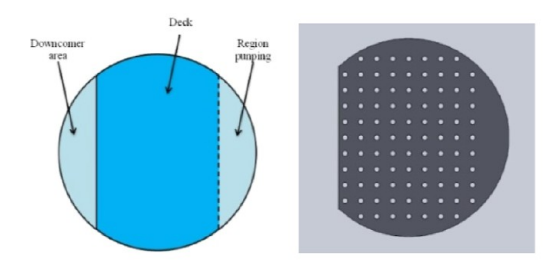
By leveraging advanced simulation tools and thermodynamic modeling, the designed distillation column achieves high-purity outputs and efficient operation. The methodology and results reflect the practical and industrial significance of the process, offering a robust framework for the separation of benzene and toluene. The detailed profiles of concentration, temperature, pressure, and flow rates provided in the Supporting Information serve as valuable references for engineers and practitioners in the field.

The successful application of AspenOne software, combined with the NRTL model and BUMDA optimization algorithm, demonstrates the effectiveness of integrating advanced computational tools with rigorous design principles. This approach not only ensures the technical feasibility of the distillation process but also enhances its practical implementation in industrial settings, contributing to improved efficiency and sustainability in chemical processing.

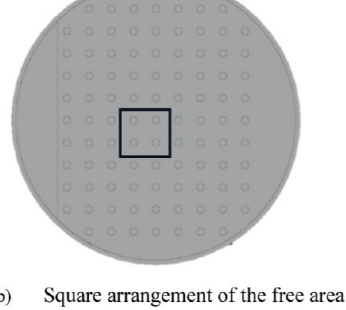
**3.2. CAD Design.** The second step of the methodology proposed in this paper involves the mechanical design of the tray and distillation column utilizing Computer-Aided Design (CAD) software, specifically SolidWorks. The dimensions for the CAD model of the tray and distillation column were derived from the case study detailed in Section 2.1, with calculations performed using AspenOne. The selected construction material is stainless steel 316L.

Detailed engineering drawings are provided in Figure 2, illustrating the downcomer area, the deck, the pumping area, the arrangement of the tray holes, the tray sieve within the column, pressure drop and the stripping stages under investigation. Table 2 compiles the parameters employed in the design of the sieve tray. Key design considerations included the column diameter, determined through rigorous simulation in AspenOne, a tray spacing of 0.3048 m, and a downcomer area ranging from 5 to 15% of the total deck area, with the remainder designated as the bubbling area. These parameters adhere to the conventional standards used in the mechanical design of industrial distillation columns.

- Design Process: The CAD model was meticulously developed in SolidWorks, ensuring precise alignment with the dimensions calculated using AspenOne. The structural integrity and feasibility of the design were evaluated against industry standards.
- Material Selection: Stainless steel 316L was chosen for its excellent corrosion resistance and durability, which are critical in distillation processes.
- Key Design Features: Downcomer Area: This component facilitates the flow of liquid between trays and was designed to occupy 5 to 15% of the total deck area, Deck and Bubbling Area: The remaining deck area is designated for vapor—liquid contact, essential for effective distillation.
- Tray Holes Arrangement: Optimized for uniform distribution and efficiency in heat transfer.
- Pumping Area and Stripping Stages: Detailed to ensure effective separation and operational efficiency.
- 3.2.1. Simulation and Validation. Comprehensive simulations were conducted using AspenOne to validate the design parameters, ensuring that the dimensions and configurations meet the required performance criteria. The simulation results were cross-referenced with industry standards to confirm accuracy and reliability. By adhering to these detailed design steps and parameters, the mechanical design ensures operational



a) Layout of the sieve plate used in the CFD simulations.





c) Tray sieve inside the column



Distillation column stripping stages studied.

Figure 2. Mechanical design of the tray and distillation column in SolidWorks.

Table 2. Tray Sieve Specification

| parameter           | value              |
|---------------------|--------------------|
| tray diameter (m)   | 0.208              |
| tray spacing (m)    | 0.304              |
| holes diameter (m)  | 0.05               |
| downcomer area (%)  | 5-15% (total area) |
| pitch, square (m)   | 0.015              |
| pressure drop (atm) | 0.7                |

efficiency and aligns with traditional practices in industrial distillation column design. 67,68

3.3. CFD Simulation. The third step of our proposed methodology involves setting the initial conditions of the system under investigation and determining the number of particles required to resolve the velocity and temperature profiles accurately. This step is crucial for obtaining precise simulation results and understanding the system's dynamics in detail.

As detailed in Section 2.1, we focus on stage 8 (referred to as stage N), with the understanding that the liquid and vapor inlet data for this stage correspond to stages 7 (N - 1) and 9 (N + 1), respectively. The liquid enters stage 8 via the downcomer from stage 7. Simultaneously, the vapor from stage 9 enters the lower part of stage 8 through orifices, rising up the column and overcoming the resistance of the liquid within the stage. This process prevents the liquid from descending through the orifices.

Within stage 8, momentum and heat transfer occur as the vapor, in the form of bubbles, comes into intimate contact with the liquid. This interaction is crucial for the accurate simulation of the system's behavior. The vapor eventually rises to stage 7 (N -1), while the liquid descends to stage 9 (N + 1).

To analyze this system numerically, we conducted simulations using a total of 7,261,750 fluid particles. These particles are categorized as follows:

- 1,386,940 bound particles: These represent the stationary boundaries and structures within the system.
- 4,230,940 liquid particles: These simulate the liquid phase, capturing the dynamic behavior of the liquid within the column.
- 1,643,870 vapor particles: These represent the vapor phase, allowing for detailed tracking of vapor movement and interactions.

The simulation represents 60 s of real time and was completed in 17.5 h using the NVIDIA GeForce 3060 GPU at TecNM/ ITESI. The number of particles was chosen based on the processing capabilities of the GPU, as the simulation was GPUaccelerated. This high particle count ensures a detailed and accurate representation of the system's fluid dynamics, which is essential for capturing the intricate interactions between the liquid and vapor phases.

The particle count in our work is approximately five times higher than that used in Eulerian methods for similar cases, which typically involve between 100,000 cells<sup>26</sup> and 1.3 million cells.<sup>13</sup> This substantial increase in particle count is justified by the need for higher resolution in the simulation. Higher particle counts lead to more accurate and detailed results, particularly in complex systems where fine-scale interactions are critical.

3.3.1. Simulation Results and Performance. The simulation results provide detailed insights into the velocity and temperature profiles within the column. By capturing the intricate interactions between liquid and vapor phases, the SPH method allows for a comprehensive understanding of the system's behavior under various conditions. The performance metrics,

including the total simulation time and particle count, demonstrate the efficiency and scalability of the SPH method when combined with GPU acceleration.

The third step of our methodology, involving the definition of initial conditions that Figure 3 is shown, and the particle

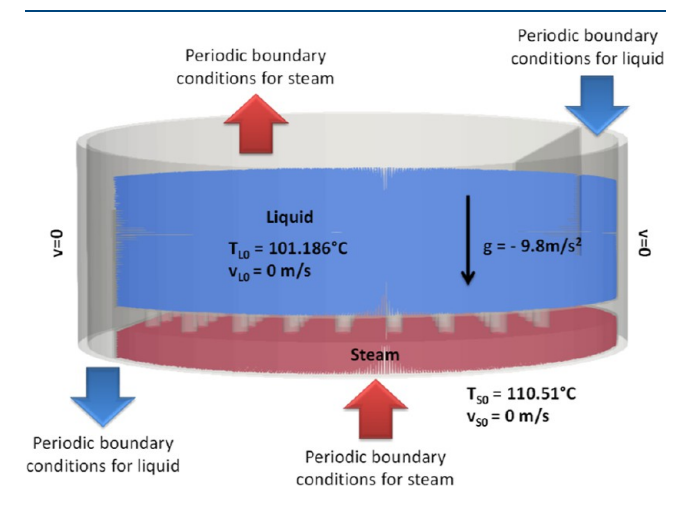


Figure 3. Stage design and initial conditions of simulation.

resolution, that is critical for achieving accurate and detailed simulations. By leveraging the SPH method and GPU acceleration, we are able to overcome the limitations of traditional Eulerian methods, providing a more efficient and scalable approach to simulating complex fluid dynamics systems.

## 4. ANALYSIS OF RESULTS

In this study, we conduct a comprehensive analysis of the flow regime, weeping phenomena, velocity profiles, and temperature distribution in different regions of the sieve tray. The primary objective is to elucidate how variations in tray geometry, specifically modifications to the deck area percentage, impact the tray's performance. The insights gained from this analysis are essential for guiding the design and operation of distillation columns, particularly in optimizing the trade-offs between pressure drop, phase contact efficiency, and energy consumption.

**4.1. Flow Regimes.** Flow regimes within sieve trays are characterized by the interaction between the vapor and liquid phases, which can range from well-mixed bubbly flows to more chaotic spray flows. These regimes are influenced by the superficial gas velocity, liquid flow rate, and the physical configuration of the tray, including the size and distribution of holes. Three distinct flow regimes are typically observed: bubbly flow regime, mixed froth regime, and spray regime. These regimes span a continuum from gas-dispersed bubbly flow to liquid-dispersed spray flow, each with unique characteristics that affect the efficiency of mass and heat transfer within the column.

Most research has focused on the bubbly flow regime because it is relatively tractable because the gas—liquid interaction is stable and the dispersion height is uniform. This regime generally reduces the risk of liquid entrainment, provides constant phase contact, but the rise of the bubbles is laminar. As the gas surface velocity increases, the system transitions to more complex flow regimes, such as mixed foam and spray regimes, which are characterized by increased turbulence and chaotic phase interactions. In addition, the flow regimes that occur at the

industrial scale are mixed froth regime and spray regime due that enhance mass and heat transfer phenomena.

In this study, the SPH method was employed to simulate the flow regimes within the sieve tray, providing detailed insights into the dynamic behavior of the system. Figure 4 presents a comparative analysis of the flow regimes obtained at different time intervals. In Figure 4a, the evolution of flow regimes over time is depicted, showing a clear transition from bubbly flow to spray flow. This transition is marked by a progressive increase in turbulence, which leads to more chaotic and less predictable phase interaction, increase interaction between phases.

Figure 4b provides a detailed comparison of flow regimes for different modifications to the sieve tray geometry, maintaining the surface velocity of the vapor constant. For the case with an 85% deck area, the system remains in the bubbly flow regime throughout the simulation, indicating a relatively stable and uniform phase distribution. However, as the deck area increases to 90% and 95%, the flow regime shifts toward the spray regime by the end of the simulation. This shift is indicative of increased turbulence and phase interaction, which can enhance mass and heat transfer.

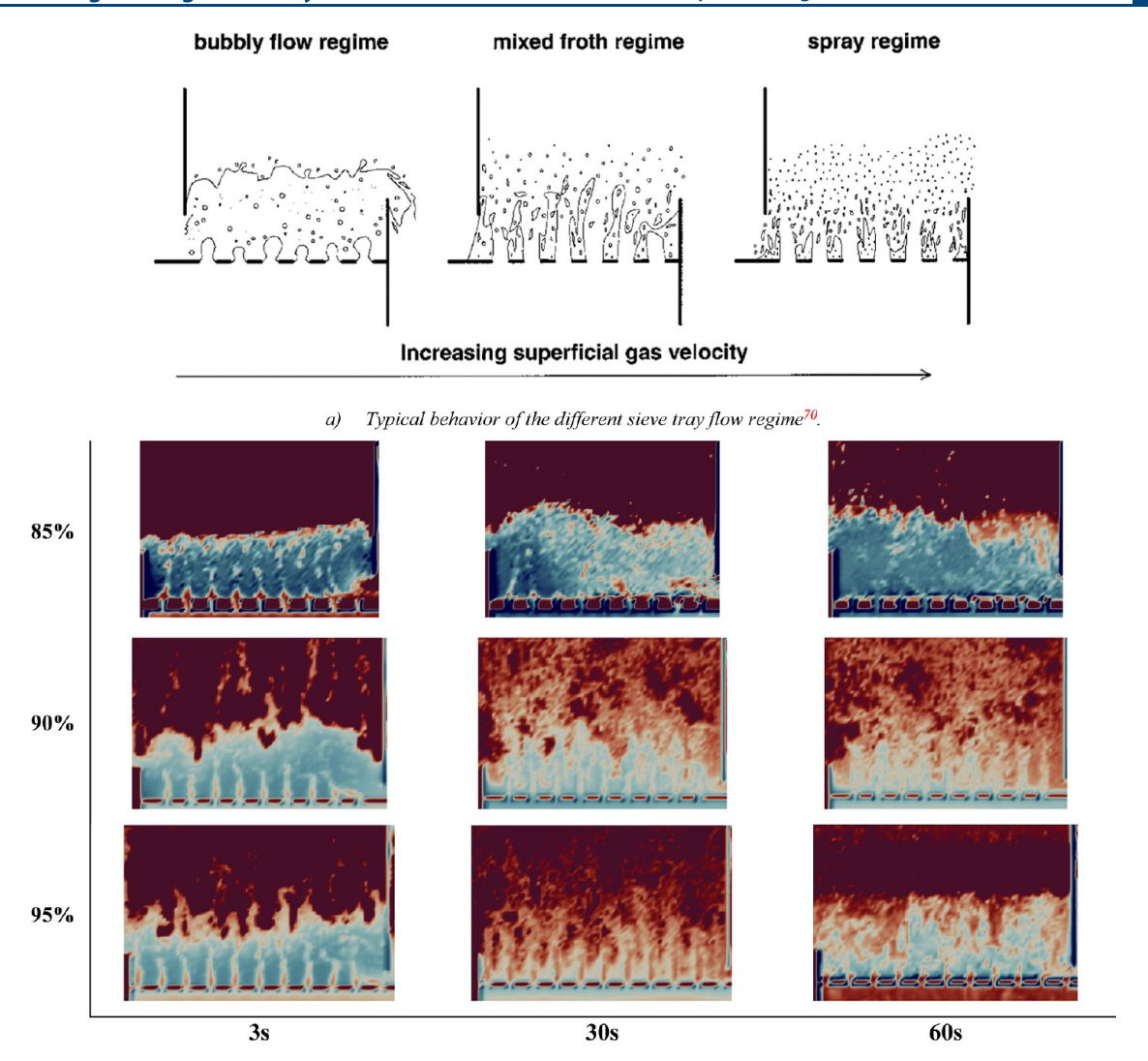
The robustness of the SPH method is highlighted by its ability to accurately simulate the full spectrum of flow regimes within the tray, from stable bubbly flow to chaotic spray flow. This capability is particularly important for predicting the performance of sieve trays under varying operational conditions, as it allows for the identification of optimal design parameters that balance phase contact efficiency with pressure drop and energy consumption.

It is important to note that in all SPH simulations; the liquid and vapor velocities were held constant across all cases, corresponding to the conditions provided by AspenOne (see Table 1). This consistency allows for a direct comparison of how changes in tray geometry influence the flow regime and overall performance of the tray. The observed changes in flow regime are attributed to the variations in deck area, with larger deck areas promoting more turbulent and chaotic flow patterns.

**4.2. Liquid–Vapor Flow Patterns.** Flow patterns within the sieve tray are a critical determinant of the tray's performance, as they directly influence the distribution of phases, the extent of phase interaction, and the overall efficiency of mass and heat transfer. The velocity vectors and liquid fraction on the horizontal bottom and top planes relative to the deck area are shown in Figure 5 for the three study cases. The analysis was conducted at three distinct time points: 3 s, 30 s, and 60 s, to capture the evolution of flow patterns over time.

For the 85% deck area case, the velocity vectors near the downcomer indicate a strong directional flow toward the liquid overflow, both on the bottom and top planes. This suggests a highly organized flow pattern where the liquid phase dominates near the downcomer, with minimal of vapor flow. The presence of stagnant zones on the top plane, particularly near the downcomer and column wall, is indicative of poor phase mixing and limited vapor rise. These stagnant zones, characterized by the absence of velocity vectors, persist across all three analyzed time points, suggesting that the flow pattern is relatively stable but not conducive to efficient phase contact.

On the bottom plane, the liquid is observed to flow preferentially through regions where vapor flow is absent, creating distinct channeling zones. This channeling effect is undesirable as it leads to uneven phase distribution and reduced mass transfer efficiency. The correlation between phase distribution and the velocity field is evident, with the vapor



b) Progress of the flow regime in the sieve tray, for different percentages of the deck area.

Figure 4. Comparison of sieve tray flow rates obtained with the SPH method with respect to time.

phase being entrained by the liquid near the tray, resulting in a vapor phase distribution dominated by the liquid's velocity field. This behavior is characteristic of the bubbly flow regime, as depicted in Figure 4, and underscores the limitations of this regime in achieving efficient phase contact and heat transfer.

For the 90% deck area case, the flow pattern becomes more complex, with increased phase interaction and improved homogenization of the liquid and vapor phases. On the bottom plane, the liquid phase remains dominant until 60 s, with the presence of homogenization zones near the downcomer where both phases interact more evenly. On the top plane, the vapor phase is observed to migrate toward the column walls, driven by the liquid flow toward the overflow. This lateral migration of the vapor phase is indicative of increased phase interaction and a more turbulent flow pattern, which can enhance mass and heat transfer but may also increase the risk of liquid entrainment.

The reduction in liquid channeling near the downcomer, particularly at 60 s, suggests that the 90% deck area design offers a better balance between phase distribution and flow stability compared to the 85% case. The improved homogenization observed in this case is a positive indicator of enhanced phase contact efficiency, which is critical for optimizing the performance of the distillation column.

In the 95% deck area case, the flow pattern undergoes a significant transformation, with a marked reduction in channeling near the downcomer and a more chaotic velocity field. The proximity of the holes to the downcomer plays a key role in this transformation, as it facilitates more direct phase interaction and reduces the formation of stagnant zones. At 30 s, phase homogenization is initiated on the bottom plane, with velocity vectors exhibiting turbulent behavior indicative of the onset of the spray regime that promotes contact between phases.

On the top plane, the vapor phase is more evenly distributed, with vapor-dominated zones near the column wall gradually dissipating as the system approaches equilibrium. By 60 s, the flow pattern becomes highly chaotic on both the top and bottom planes, with a substantial reduction in channeling and a more uniform phase distribution. This behavior is characteristic of the spray regime, as described in Figure 4. This suggests that the 95% deck area design offers the best performance in terms of phase contact efficiency and heat transfer.

The analysis of flow patterns clearly demonstrates that increasing the deck area from 85–95% leads to more favorable flow conditions, with reduced channeling, improved phase homogenization, and a transition to the spray regime. These findings highlight the importance of optimizing tray geometry to

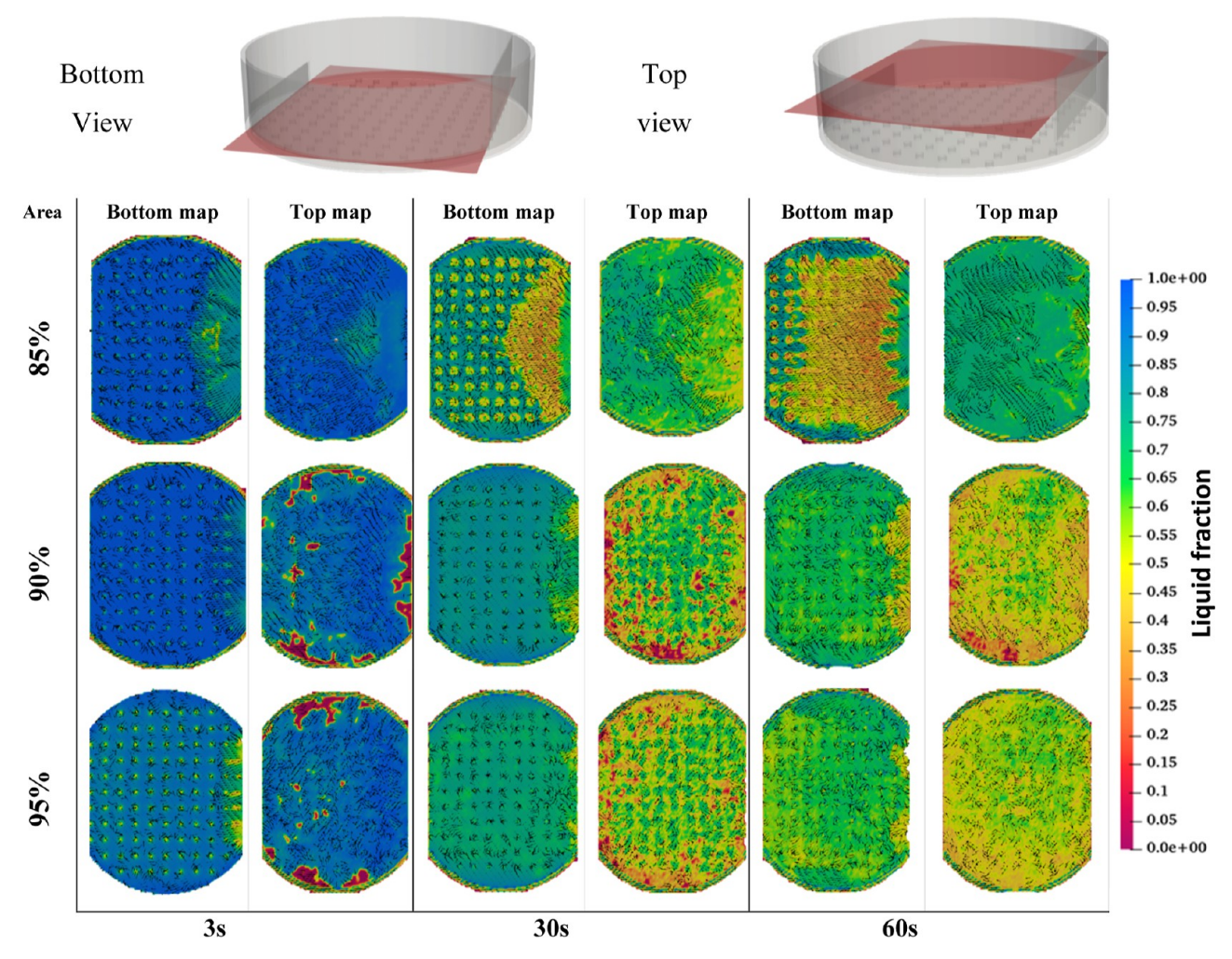


Figure 5. Liquid velocity vectors and liquid fraction contour on horizontal bottom and top plane the deck tray.

achieve the desired balance between phase distribution, pressure drop, and energy efficiency.

**4.3. Weeping Phenomena.** Weeping, or the downward leakage of liquid through tray holes, is a critical phenomenon in tray distillation columns that can significantly impact the column's efficiency. Weeping occurs when vapor flow is insufficient to sustain the liquid on the tray, causing the liquid to drain through the holes instead of being properly dispersed and contacted with the vapor phase. This phenomenon is particularly problematic in the bubbly flow regime, where vapor flow is relatively low, and pressure drop fluctuations across the tray can exacerbate weeping.

In this study, the weeping phenomenon was analyzed for sieve trays with 85%, 90%, and 95% deck areas, with a focus on understanding how tray geometry influences weeping behavior. Figure 6 illustrates liquid weeping from the deck holes in the bottom view of the tray for the three study cases, with blue indicating the liquid fraction. The analysis was conducted at 60 s, capturing the steady-state behavior of the system.

For the 85% deck area case, a high weeping rate is observed, with liquid flowing entirely through several holes, particularly those near the downcomer. This high weeping rate is undesirable, as it reduces the contact time between the liquid and vapor phases, leading to inefficient mass and heat transfer. The presence of large weeping zones near the downcomer indicates that the 85% deck area design is prone to significant

liquid losses, which can compromise the overall performance of the distillation column, due to liquid accumulation in the lower stage.

In contrast, the 90% and 95% deck area cases exhibit significantly lower weeping rates, with liquid particles adhering to the solid on the bottom side of the sieve tray. This behavior suggests that the increased deck area helps to reduce weeping by providing more surface area for vapor-liquid interaction and by promoting better phase dispersion. The lower weeping rate in these cases is likely due to two mechanisms: (1) the upward vapor flow from stage N + 1 entrains the liquid toward stage N, (2) the liquid from the N + 1 stage splashes in the form of finer droplets on the bottom of the N stage. In both cases a liquid film may form on the bottom face of the tray. This behavior is consistent with the spray regime and favors mass and heat transfer on the plate. Therefore, decreasing the exudation rate is desirable in the operation of plate distillation columns. In this sense, the best performance is presented by the designs with 90 and 95% of deck area.

**4.4. Temperature Distribution Analysis.** The transient analysis of temperature distribution was conducted for three study cases with deck areas of 85%, 90%, and 95%. The initial conditions in the simulations were derived from AspenOne for stages N-1 and N+1, corresponding to temperatures of 101.186 and 110.51  $^{\circ}$ C, respectively. The focus of the analysis was on stage 8 (stage N), where thermal equilibrium is achieved

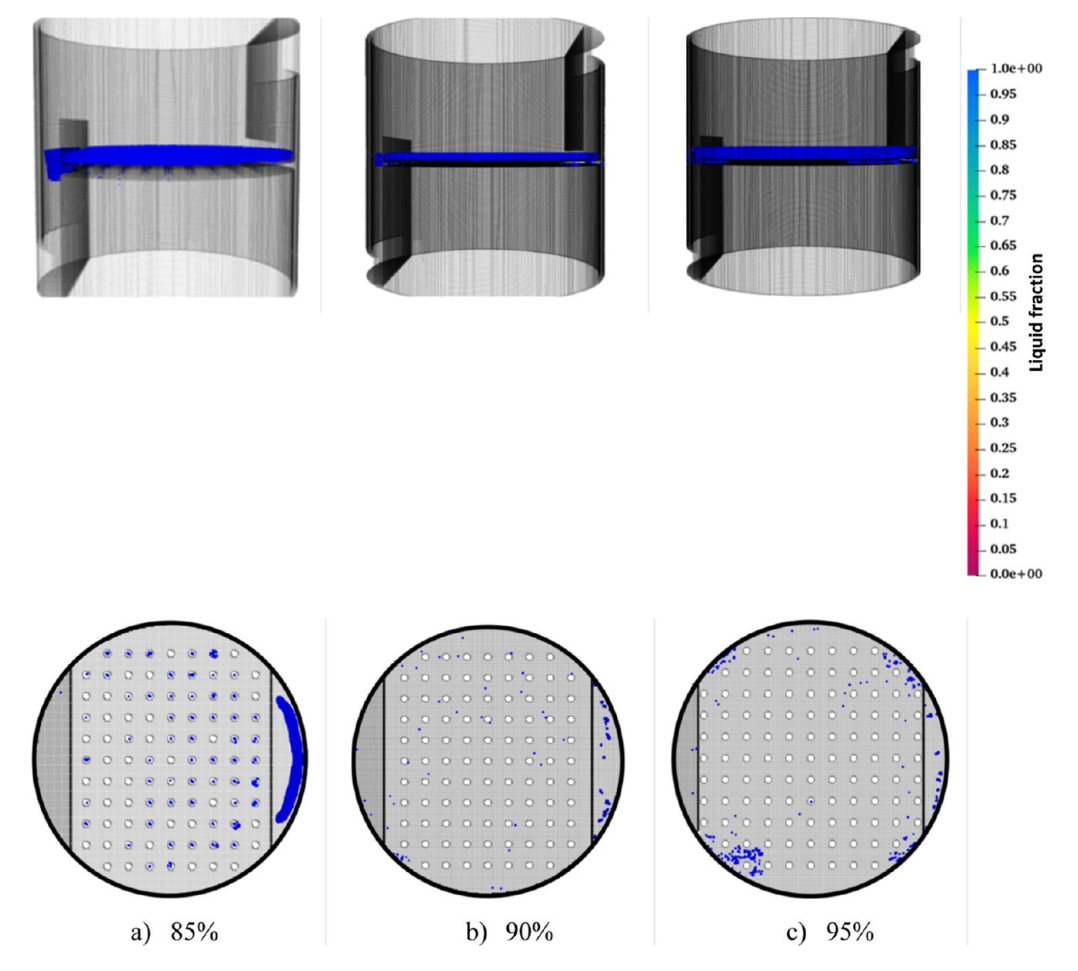


Figure 6. Liquid weeping from the deck holes in the bottom view of tray.

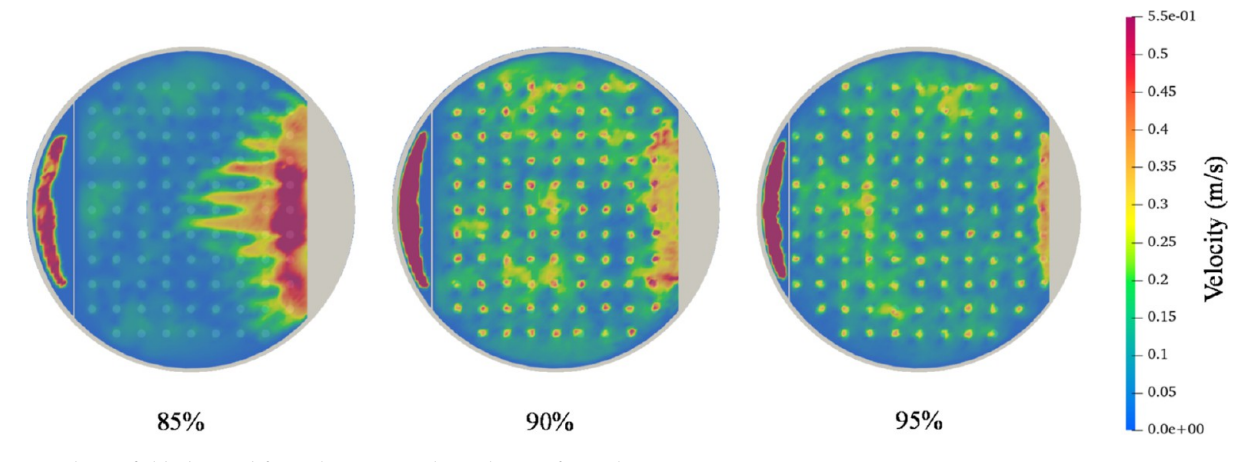


Figure 7. Velocity field obtained from the numerical simulations for each case.

at 105.50 °C. This key data is summarized in Table 1. The numerical simulations provided critical insights into the heat transfer rate and Reynolds number fields, which were used to analyze the thermal flow distribution across different regions of the stage.

The velocity field immediately above the sieve tray, illustrated in Figure 7, was evaluated for each deck area configuration (85%, 90%, and 95%). The velocity field for the 85% deck area case exhibits a significantly different pattern compared to the 90% and 95% cases. Specifically, in the 85% configuration, the velocity field demonstrates a distinct mean distribution within

the channels formed between the holes, creating well-defined patterns flow on the sieve tray. This distribution pattern suggests a localized flow concentration that is influenced by the spatial configuration of the holes. As the deck area increases from 85–95%, the extent of this concentrated flow distribution diminishes, as depicted in Figure 7. The SPH (Smoothed Particle Hydrodynamics) numerical results reveal that the flow generated through the holes plays a critical role in shaping the velocity distribution on the sieve tray, with bigger deck areas leading to a more uniform flow distribution.

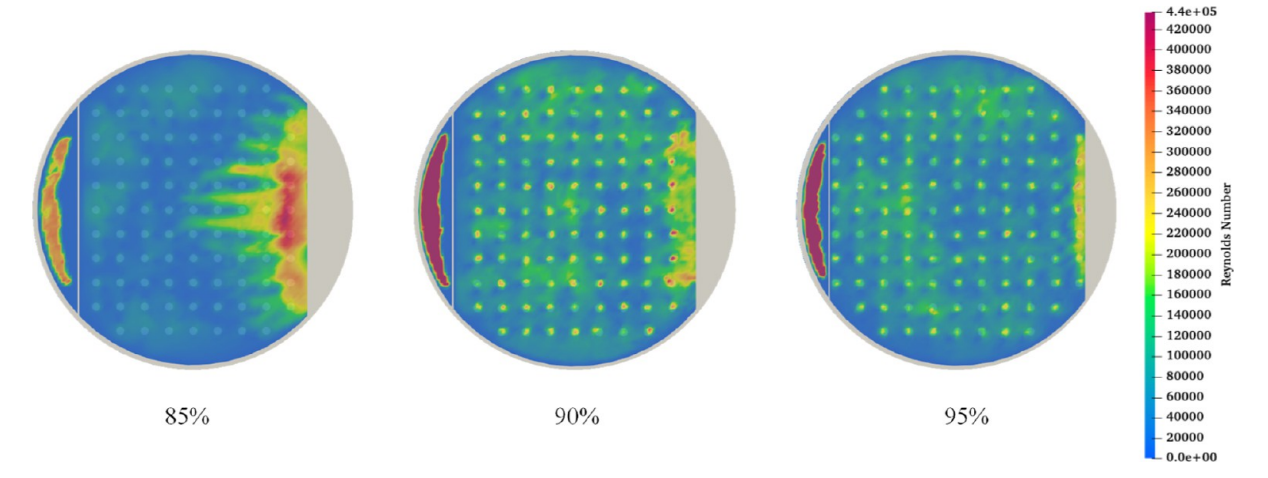


Figure 8. Reynolds field obtained from the numerical simulations for each case.

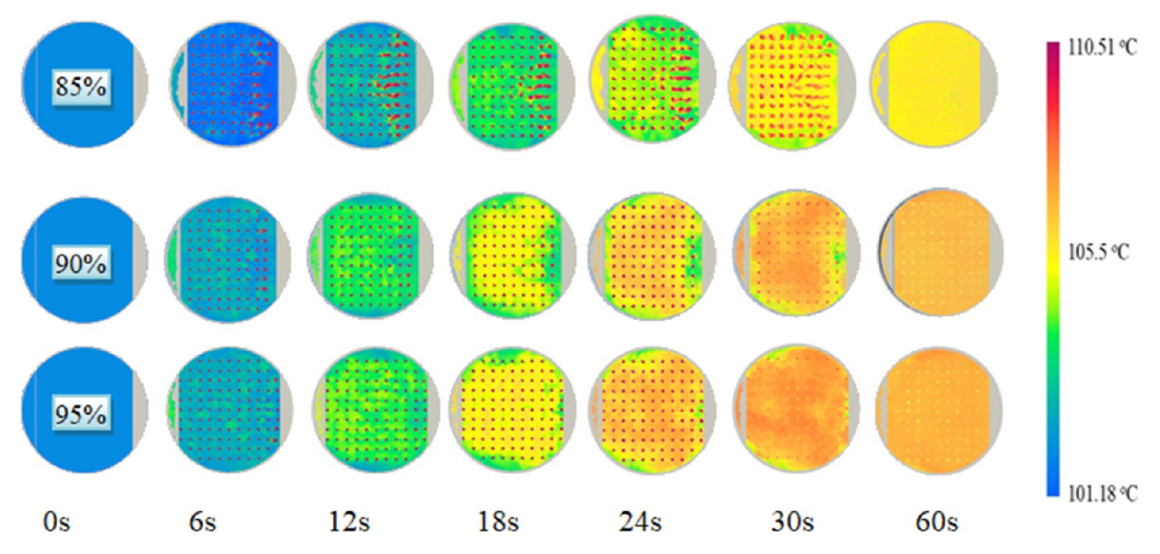


Figure 9. Temperature distribution of the tray and behavior throughout the simulation, for 85, 90 and 95% of the deck area.

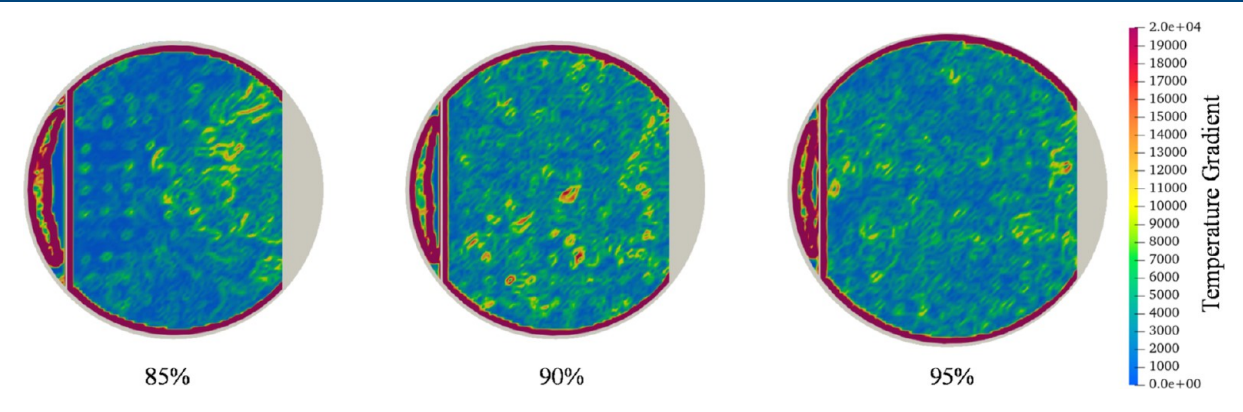


Figure 10. Temperature gradient obtained from SPH numerical simulations.

To further quantify the flow characteristics, the flow regime in the various zones of the tray was determined using the Reynolds number, calculated as Re = vD/v, where v represents the velocity vector, D denotes the characteristic length of the deck area, and v is the kinematic viscosity of the mixture. The maximum Reynolds number, observed just above the tray, was nearby  $4.4 \times 10^5$ , as shown in Figure 8. This relatively low Reynolds number indicates that the flow near the tray remains in the turbulent regime for all configurations. The red zone observed on the left

side of Figures 7 and 8 corresponds to the downcomer area, which is excluded from the tray analysis due to its distinct flow dynamics.

Figure 9 presents the temperature distribution across the tray and its evolution throughout the simulation for the 85%, 90%, and 95% deck area configurations, measured at various time intervals between 0 and 60 s. The color gradients, with red representing higher temperatures and blue indicating lower temperatures, provide a visual representation of the thermal

behavior on the tray. During the initial phase of 0 to 30 s, the highest temperatures are concentrated around the holes, indicating localized heat accumulation due to the intense phase interactions at these points. However, by 60 s, the temperature distribution across the tray becomes more uniform, signifying the approach to thermal equilibrium.

For the 85% deck area design, the analysis indicates a suboptimal temperature distribution. During the first 30 s, the highest temperatures are observed around the holes, suggesting that the heat transfer process is initially dominated by the localized phase interactions in these regions. As time progresses to 60 s, the temperature across the tray becomes more homogeneous, especially in the 85% deck area scenario. This homogeneity indicates that the heat transfer process eventually equilibrates, but the initial nonuniform distribution underscores the challenge of achieving optimal thermal performance with a reduced deck area. In all cases, at the 60 s mark, thermal equilibrium is achieved at the holes. This phenomenon can be attributed to the higher heat transfer rates near the holes, driven by the intimate contact between the liquid and vapor phases, which accelerates the thermal equilibrium process in these regions.

In Figure 10, the temperature gradient for each analyzed case at 60 s is shown. The SPH numerical results for the 85% deck area reveal that the temperature gradient is closely linked to the velocity field, highlighting the interplay between fluid dynamics and thermal behavior on the tray. A correlation can be observed between the velocity distribution in Figure 7 and the temperature distribution in Figure 9, particularly near the downcomer. In regions farther from the downcomer, the temperature distribution is more uniform, indicating that the influence of localized flow dynamics diminishes with distance from the downcomer.

On the other hand, for the 90% and 95% deck area cases, the temperature distribution becomes more heterogeneous, with an expanded area where the temperature gradient exhibits moderate values (≈11,000) compared to the 85% case. This increased gradient suggests an enhancement in heat transfer efficiency, leading to a more effective redistribution of thermal energy across the tray. The larger temperature gradient in these cases not only improves the overall heat transfer process but also reduces the time required to achieve thermal equilibrium, indicating a potential advantage in scenarios where rapid thermal stabilization is desired. This improvement in heat transfer performance, however, must be balanced against the potential for increased pressure drop and flow resistance associated with higher deck area configurations.

Additionally, the equations proposed by Bennett et al.<sup>71</sup> and Van Batten and Krishna<sup>21</sup> were used to determine representative parameters of the hydrodynamic behavior in tray columns. Table S3 presents the results for parameters such as vapor velocity in the orifice (Vh), the ratio between the total area of the orifices and the deck area (Ath/Adeck), bubble rise velocity (Vrise), and Reynolds number in the orifice (Reh). This information was added in the Supporting Information. These parameters were determined for each proposed deck area percentage. It is observed that orifice velocity, bubble rise velocity, and Reynolds number decrease as the deck area percentage increases. This favors heat transfer, as the decrease in vapor velocity and bubble rise velocity results in a shorter residence time in the equilibrium stage, leading to increased intimate contact between the liquid and vapor phases. This can be corroborated with Figures 5 and 6. On the other hand, the

ratio between the deck area and the bubbling area (total orifice area) is greater when the deck area percentage is 95%. This explains why the hydrodynamic performance and temperature profile yield the best results. The obtained results are consistent with the ranges reported in the literature.<sup>71</sup>

### 5. CONCLUSIONS

The analysis of sieve trays in distillation columns reveals that tray geometry, particularly deck area percentage, significantly influences hydrodynamics, heat transfer, and operational phenomena like weeping. As the deck area increases from 85-95%, the flow regime shifts from bubbly to a more turbulent spray regime, enhancing phase interaction and improving mass and heat transfer but increasing pressure drop. The velocity vector analysis showed that larger deck areas reduce stagnant zones and promote better vapor distribution, optimizing column performance. The study found that weeping is notably impacted by deck area percentage. The 85% deck area exhibited higher weeping rates, reducing tray efficiency, while 90% and 95% designs minimized weeping due to improved phase dispersion and reduced vapor entrainment, enhancing operational efficiency. Temperature distribution analysis revealed that a smaller deck area (85%) results in localized nonuniformities due to concentrated flow near tray holes, which gradually even out as the system reaches equilibrium. Larger deck areas (90% and 95%) displayed more heterogeneous flow and temperature profiles, leading to enhanced heat transfer efficiency but potentially increased pressure drop. The study validated the Smoothed Particle Hydrodynamics (SPH) method's effectiveness in capturing complex flow regimes and phase interactions under varying geometric configurations. These findings underscore the importance of optimizing tray geometry for balanced flow conditions, heat transfer, and efficiency. Future research should consider additional parameters, like hole size and distribution, to further optimize tray designs.

# ASSOCIATED CONTENT

#### **Supporting Information**

The Supporting Information is available free of charge at https://pubs.acs.org/doi/10.1021/acs.iecr.4c03313.

Table S1 temperature and pressure profiles of a benzene-toluene distillation column. Table S2 liquid mole fraction profile of a benzene-toluene distillation column. Table S3 parameters used to quantify the performance of the sieve plate (PDF)

# AUTHOR INFORMATION

#### **Corresponding Author**

Rodolfo Murrieta-Dueñas — Departamento Ingeniería Química, Tecnológico Nacional de México/ Campus Irapuato, Irapuato, Guanajuato 36821, Mexico; orcid.org/0000-0001-5759-2500; Email: rodolfo.md@irapuato.tecnm.mx

#### **Authors**

Jazmín Cortez-González — Departamento Ingeniería Química, Tecnológico Nacional de México/ Campus Irapuato, Irapuato, Guanajuato 36821, Mexico

Carlos Enrique Alvarado-Rodríguez — Departamento de Ingeniería Química, Universidad de Guanajuato, Campus Guanajuato, Guanajuato 36500, Mexico

Juan Gabriel Segovia-Hernández – Departamento de Ingeniería Química, Universidad de Guanajuato, Campus Guanajuato, Guanajuato 36500, Mexico; orcid.org/0000-0003-4175-9809

Salvador Hernández — Departamento de Ingeniería Química, Universidad de Guanajuato, Campus Guanajuato, Guanajuato 36500, Mexico

Roberto Gutiérrez-Guerra — Universidad Tecnologica de Leon (UTLeon, Blvd. Universidad Tecnologica 225, Leon, Guanajuato 37670, Mexico

Complete contact information is available at: https://pubs.acs.org/10.1021/acs.iecr.4c03313

#### Notes

The authors declare no competing financial interest.

#### REFERENCES

- (1) Olujić, Ž.; Kaibel, B.; Jansen, H.; Rietfort, T.; Zich, E.; Frey, G. Distillation column internals/configurations for process intensification. *Chem. Biochem. Eng. Q.* **2003**, *17* (4), 301–309.
- (2) Masoumi, M. E.; Kadkhodaie, S. Optimization of energy consumption in sequential distillation column. *Int. J. Chem. Environ. Eng.* **2012**, *6* (1), 67–80.
- (3) Rodríguez-Ángeles, M. A.; Gómez-Castro, F. I.; Segovia-Hernández, J. G.; Uribe-Ramírez, A. R. Mechanical design and hydrodynamic analysis of sieve trays in a dividing wall column for a hydrocarbon mixture. *Chem. Eng. Process.* **2015**, *97*, 55–65.
- (4) Petlyuk, F. B.; Platonov, V. M.; Slavinski, D. M. Thermodynamically optimal method of separating multicomponent mixtures. *Int. J. Chem. Eng.* **1965**, *5*, 555–561.
- (5) Amminudin, K. A.; Smith, R.; Thong, D. Y.-C.; Towler, G. P. Design and optimization of fully thermally coupled distillation columns: Part 1: preliminary design and optimization methodology. *Chem. Eng. Res. Des.* **2001**, *79*, 701–715.
- (6) Gómez-Castro, F. I.; Rodríguez-Ángeles, M. A.; Segovia-Hernández, J. G.; Gutiérrez-Antonio, C.; Briones-Ramírez, A. Optimal designs of multiple dividing wall columns. *Chem. Eng. Technol.* **2011**, *34*, 2051–2058.
- (7) Weinfeld, J. A.; Owens, S. A.; Eldridge, R. B. Reactive dividing wall columns: A Comprehensive review. *Chem. Eng. Process.* **2018**, *123*, 20–33
- (8) Malvin, A.; Chan, A.; Lau, P. L. CFD study of distillation sieve tray flow regimes using the droplet size distribution technique. *J. Taiwan Inst. Chem. Eng.* **2014**, *45* (4), 1354–1368.
- (9) Mehta, B.; Chuang, K. T.; Nandakumar, K. Model for liquid phase flow on sieve trays. *Chem. Eng. Res. Des.* 1998, 76 (7), 843–848.
- (10) Yu, K. T.; Yuan, X. G.; You, X. Y.; Liu, C. J. Computational fluid-dynamics and experimental verification of two-phase two-dimensional flow on a sieve column tray. *Chem. Eng. Res. Des.* **1999**, 77 (6), 554–560.
- (11) Liu, C. J.; Yuan, X. G.; Yu, K.; Zhu, X. J. A fluid—dynamic model for flow pattern on a distillation tray. *Chem. Eng. Sci.* **2000**, *55* (12), 2287—2294.
- (12) Zarei, A.; Hosseini, S. H.; Rahimi, R. CFD and experimental studies of liquid weeping in the circular sieve tray columns. *Chem. Eng. Res. Des.* **2013**, *91* (12), 2333–2345.
- (13) Krishna, R.; Van Baten, J. M.; Ellenberger, J.; Higler, A. P.; Taylor, R. CFD simulations of sieve tray hydrodynamics. *Chem. Eng. Res. Des.* 1999, 77 (7), 639–646.
- (14) Li, Q.; Li, L.; Zhang, M.; Lei, Z. Modeling flow-guided sieve tray hydraulics using computational fluid dynamics. *Ind. Eng. Chem. Res.* **2014**, 53 (11), 4480–4488.
- (15) Zarei, A.; Hosseini, S. H.; Rahimi, R. CFD study of weeping rate in the rectangular sieve trays. *J. Taiwan Inst. Chem. Eng.* **2013**, 44 (1), 27–33.
- (16) Bernard, J. D. T.; Sargent, R. W. H. The hydrodynamic performance of a sieve plate distillation column. *Trans. Inst. Chem. Eng.* **1966**, *44*, 314.

- (17) Rahimi, R.; Sotoodeh, M. M.; Bahramifar, E. The effect of tray geometry on the sieve tray efficiency. *Chem. Eng. Sci.* **2012**, *76*, 90–98.
- (18) Sun, J.; Luo, X.; Jiang, S.; Wang, W.; Lyu, H.; Wang, P.; Gao, H. Computational Fluid Dynamics Hydrodynamic Analysis of a Cross-Orthogonal Fixed-Valve Tray. *Chem. Eng. Technol.* **2014**, *37* (3), 383–301
- (19) Li, X.; Yang, N.; Sun, Y.; Zhang, L.; Li, X.; Jiang, B. Computational fluid dynamics modeling of hydrodynamics of a new type of fixed valve tray. *Ind. Eng. Chem. Res.* **2014**, 53 (1), 379–389.
- (20) Kállai, V.; Mizsey, P.; Szepesi, G. L. CFD Investigation of Dry Tray Pressure Drop of Perforated Trays without Downcomer. *Period. Polytech., Chem. Eng.* **2023**, *67* (2), 310–315.
- (21) Van Baten, J. M.; Krishna, R. Modelling sieve trays hydraulics using computational fluid dynamics. *Chem. Eng. J.* **2000**, 77, 143–151.
- (22) Movahedi, P. M.; Rahimi, R. Hydrodynamics of sieve tray distillation column using CFD simulation. *J. Chem. Pet. Eng.* **2015**, 49 (2), 119–129.
- (23) Singh, S. CFD simulations of benzene-toluene system over sieve tray. *Inter. J. Eng. Sci. Emerging Tech.* **2012**, *3*, 81–89.
- (24) Canchola-López, P. G.; Vázquez-Hernández, A. E.; Cortez-González, J.; Murrieta-Dueñas, R.; Gutiérrez-Guerra, R.; Alvarado-Rodríguez, C. E. Numerical simulation of the LV equilibrium within a stage in a distillation column using CFD. *Comput.-Aided Chem. Eng.* **2023**, *52*, 1347–1352.
- (25) Zarei, T.; Abedini, E.; Rahimi, R.; Khorshidi, J. Computational fluid dynamics on the hydrodynamic characteristics of the conical cap tray. *Korean J. Chem. Eng.* **2017**, *34*, 969–976.
- (26) Malvin, A.; Chan, A.; Lau, P. L. Large eddy simulation of distillation sieve tray hydrodynamics using volume-of-fluid (VOF) multiphase model. In *Proceedings of the World Congress on Engineering and Computer Science*; WCECS, 2010; pp 20–22.
- (27) Wu, Q.; Xue, J.; Hu, N.; Lai, Y.; Zhao, H.; Li, Q.; Gu, J. Open Balance Point and Dry Pressure Drop of a Rectangular Float Valve Tray: Experiment and CFD Simulation. *Ind. Eng. Chem. Res.* **2023**, *62* (48), 20844–20858.
- (28) Noriler, D.; Barros, A. A.; Maciel, M. R. W.; Meier, H. F. Simultaneous momentum, mass, and energy transfer analysis of a distillation sieve tray using CFD techniques: prediction of efficiencies. *Ind. Eng. Chem. Res.* **2010**, 49 (14), 6599–6611.
- (29) Haghshenas Fard, M.; Zivdar, M.; Rahimi, R.; Nasr Esfahani, M.; Afacan, A.; Nandakumar, K.; Chuang, K. T. CFD simulation of mass transfer efficiency and pressure drop in a structured packed distillation column. *Chem. Eng. Technol.* **2007**, *30* (7), 854–861.
- (30) Lavasani, M. S.; Rahimi, R.; Zivdar, M. Hydrodynamic study of different configurations of sieve trays for a dividing wall column by using experimental and CFD methods. *Chem. Eng. Process.* **2018**, *129*, 162–170.
- (31) Zhao, H.; Li, Q.; Yu, G.; Dai, C.; Lei, Z. Performance analysis and quantitative design of a flow-guiding sieve tray by computational fluid dynamics. *AIChE J.* **2019**, *65* (5), 16563.
- (32) Ke, T. CFD Simulation of Sieve Tray Hydrodynamics Using Openfoam, 2022.
- (33) Martínez-Herrera, G.; Cortez-González, J.; Murrieta-Dueñas, R.; Uribe-Ramírez, A. R.; Pérez-Segura, T.; Alvarado-Rodríguez, C. E. Smoothed particles hydrodynamics simulations of microbial kinetic in a stirred bioreactor with proximity impellers. *Comput. Part. Mech.* **2022**, 9 (5), 1017–1029.
- (34) Altomare, C.; Scandura, P.; Cáceres, I.; Van der, A. D.; Viccione, G. Large-scale wave breaking over a barred beach: SPH numerical simulation and comparison with experiments. *Coast. Eng.* **2023**, *185*, 9104362
- (35) Reinoso, B.; Leigh, N. W.; Barrera-Retamal, C. M.; Schleicher, D.; Klessen, R. S.; Stutz, A. M. The mean free path approximation and stellar collisions in star clusters: numerical exploration of the analytic rates and the role of perturbations on binary star mergers. *Mon. Not. R. Astron. Soc.* **2021**, *509* (3), 3724–3736.
- (36) Crespo, A. J.; Domínguez, J. M.; Rogers, B. D.; Gómez-Gesteira, M.; Longshaw, S.; Canelas, R. J. F. B.; García-Feal, O. DualSPHysics:

- Open-source parallel CFD solver based on Smoothed Particle Hydrodynamics (SPH). Comput. Phys. Commun. 2015, 187, 204–216.
- (37) Bennett, D. L.; Agrawal, R.; Cook, P. J. New pressure drop correlation for sieve tray distillation columns. *AIChE J.* **1983**, *29*, 434–442.
- (38) Gingold, R. A.; Monaghan, J. J. Smoothed particles hydrodynamics: theory and application to non-spherical stars. *Mon. Not. R. Astron. Soc.* **1977**, *181*, 375–389.
- (39) Lucy, L. B. A numerical approach to the testing of fusion process. *Astron. J.* **1977**, 82, 1013–1024.
- (40) Fourtakas, G.; Dominguez, J. M.; Vacondio, R.; Rogers, B. D. Local uniform stencil (LUST) boundary condition for arbitrary 3-D boundaries in parallel smoothed particle hydrodynamics (SPH) models. *Comput. Fluids* **2019**, *190*, 346–361.
- (41) Tafuni, A.; Domínguez, J. M.; Vacondio, R.; Crespo, A. J. C. A versatile algorithm for the treatment of open boundary conditions in Smoothed particle hydrodynamics GPU models. *Comput. Methods Appl. Mech. Eng.* **2018**, 342, 604–624.
- (42) Zhang, C.; Zhu, Y.; Lyu, X.; Hu, X. An efficient and generalized solid boundary condition for SPH: applications to multi-phase flow and fluid-structure interaction. *Eur. J. Mech. B Fluids.* **2022**, *94*, 276–292.
- (43) Liu, G. R.; Liu, M. B. Smoothed Particle Hydrodynamics a Meshfree Particle Method; World Scientific Publishing: Singapore, 2003.
- (44) Monaghan, J. J. Simulating free surface flows with sph. *J. Comput. Phys.* **1994**, *110*, 399–406.
- (45) Monaghan, J. J.; Monaghan, J. J. Smoothed particle hydrodynamics. *Annu. Rev. Astro. Astrophys.* **1992**, *30*, 543–574.
- (46) Monaghan, J. J. Smoothed particle hydrodynamics. *Rep. Prog. Phys.* **2005**, *68* (8), 1703–1759.
- (47) Monaghan, J. J. y.; Lattanzio, J. C. A refined particle method por astrophysical problems. *Astron. Astrophys.* **1985**, *149*, 135–143.
- (48) Wendland, H. Piecewise polynomial, positive definite and compactly supported radial functions of minimal degree. *Adv. Comput. Math.* **1995**, *4* (1), 389–396.
- (49) Monaghan, J. J. Simulating free surface flows with SPH. J. Comput. Phys. 1994, 110 (2), 399-406.
- (50) Becker, M.; Teschner, M. Weakly compressible SPH for free surface flows. In *Proc. of the ACM SIGGRAPH/Eurographics Symposium on Computer Animation*, 2007; pp 209–217.
- (51) Shao, S.; Lo, E. Y. M. Incompressible SPH method for simulating Newtonian and non-Newtonian flows with a free surface. *Adv. Water Resour.* **2003**, *26* (7), 787–800.
- (52) Aragón, F.; Guzmán, J. E. V.; Alvarado-Rodríguez, C. E.; Sigalotti, L. D. G.; Carvajal-Mariscal, I.; Klapp, J.; Uribe-Ramírez, A. R. Smoothed Particle Hydrodynamics Modeling of Natural Convection Around a Heated Horizontal Cylinder: A Comparison With Experiments. ASME. J. Heat Transfer. 2021, 143 (4), 042601.
- (53) Domínguez, J. M.; Fourtakas, G.; Altomare, C.; Canelas, R. B.; Tafuni, A.; García-Feal, O.; Martínez-Estévez, I.; Mokos, A.; Vacondio, R.; Crespo, A. J. C.; et al. DualSPHysics: from fluid dynamics to multiphysics problems. *Comput. Part. Mech.* **2022**, *9* (5), 867–895.
- (54) Mabssout, M.; Herreros, M. I. Runge—Kutta vs Taylor-SPH: Two time integration schemes for SPH with application to Soil Dynamics. *Appl. Math. Model.* **2013**, *37* (5), 3541–3563.
- (55) Tartakovsky, A. M.; Meakin, P. Pore scale modeling of immiscible and miscible fluid flows using smoothed particle hydrodynamics. *Adv. Water Resour.* **2006**, 29 (10), 1464–1478.
- (56) Burdick, D. L.; Leffler, W. L. Toluene and The Xylenes. In *Petrochemicals in Nontechnical Language*; PennWell: Tulsa, OK, 2010; pp 41–51.
- (57) Burdick, D. L.; Leffler, W. L. Benzene. In *Petrochemicals in Non Technical Language*; PennWell: Tulsa, OK, 2010; pp 25–40.
- (58) Phase, I.; Goyal, M.; Kadam, P.; Pandya, A.; Phase, I. I. Design of Distillation Column for Separating a Mixture of Benzene and Toluene, 2024.
- (59) Chevalier, J. L. E.; Petrino, P. J.; Gaston-Bonhomme, Y. H. Viscosity and density of some aliphatic, cyclic, and aromatic hydrocarbons binary liquid mixtures. *J. Chem. Eng. Data* **1990**, 35 (2), 206–212.

- (60) Pulido, J. L.; Maciel, M. W.; Maciel Filho, R. Nuevas perspectivas en procesos de separación: Simulación columna de destilación con integración interna de calor (CDIIC), 2010.
- (61) Renon, H.; Prausnitz, J. M. Estimation of parameters for the NRTL equation for excess Gibbs energies of strongly nonideal liquid mixtures. *Ind. Eng. Chem. Process Des. Dev.* **1969**, 8 (3), 413–419.
- (62) Desing, Simulation and Optimization Systems Division. Aspen Plus 12.1 Physical Property System, Physical Property Methods and Models; Aspen Technology, Inc.: Cambrige, MA, USA, 2003.
- (63) Cortez-González, J.; Hernández-Aguirre, A.; Murrieta-Dueñas, R.; Gutiérrez-Guerra, R.; Hernández, S.; Segovia-Hernández, J. G. Process optimization using a dynamic self-adaptive constraint handling technique coupled to a Differential Evolution algorithm. *Chem. Eng. Res. Des.* 2023, 189, 98–116.
- (64) Murrieta-Dueñas, R.; Cortez-González, J.; Hernández-Aguirre, A.; Gutiérrez-Guerra, R.; Hernandez, S.; Segovia-Hernández, J. G. Study of Performance of a Novel Stochastic Algorithm based on Boltzmann Distribution (BUMDA) coupled with self-adaptive handling constraints technique to optimize Chemical Engineering process. Comput.-Aided Chem. Eng. 2015, 37, 923–928.
- (65) Valdez, S. I.; Hernández, A.; Botello, S. A Boltzmann based estimation of distribution algorithm. *J. Inf. Sci.* **2013**, 236, 126–137.
- (66) Zielinski, K.; Laur, R. Stopping criteria for differential evolution in constrained single-objective optimization. In *Advances in Differential Evolution*; Springer Berlin Heidelberg: Berlin, Heidelberg, 2008; pp 111–138
- (67) Solari, R. B.; Bell, R. L. Fluid flow patterns and velocity distribution on commercial-scale sieve trays. *AIChE J.* **1986**, 32 (4), 640–649.
- (68) Kister, H. Z. Distillation Design; McGraw-Hill, 1992; Vol. 1, p 340.
- (69) Lockett, M. J. Distillation Tray Fundamentals; Cambridge University Press: Cambridge, UK, 1986.
- (70) Krishna, R. V. J. M.; Van Baten, J. M. Modelling sieve tray hydraulics using computational fluid dynamics. *Chem. Eng. Res. Des.* **2003**, *81* (1), 27–38.
- (71) Bennett, D. L.; Watson, D. N.; Wiescinski, M. A. New correlation for sieve-tray point efficiency, entrainmnt, and section efficiency. *AIChE J.* **1997**, *43* (6), 1611–1626.